Phase Transition of Hexatriacontane (A survey of polymer crystallization by X-ray diffraction . chapter 6)

メタデータ	言語: en
	出版者: SKP
	公開日: 2008-01-31
	キーワード (Ja):
	キーワード (En):
	作成者: Asano, Tsutomu, Mina, Md. Forhad
	メールアドレス:
	所属:
URL	http://hdl.handle.net/10297/553

Chapter 6.   Phase Transition of Hexatriacontane

6.1 Introduction

During a process of temperature change, polymer molecules exhibit phase transitions. Most of the physical transformations are followed by some energy changes which can be detected by a differential scanning calorimeter (DSC). The phase transition is also accompanied by structural changes, which can be studied by X-ray diffraction, detecting molecular orders by WAXS and higher orders by SAXS.

Linear polyethylene (PE) has a simple chemical structure which is polymerized by ethylene monomers; $[-(C_2H_4) -]$. The property of polyethylene can be well understood by comparison with the linear alkane $[C_nH_{2n+2}]$. In this chemical series, if value of n advances from 1 to 18, the substances will progress from gases to solids via liquids [1]. We call paraffin for a range of n (10 > n > 50), and PE when n > ~200. Because of the similar chemical structure, polyethylene is considered to have properties closely related to those of paraffins. Thus, the paraffin is remarked as a bridging substance to combine low molecular with high molecular (PE) materials. In order to observe the nature of linear chain molecules during the phase transitions, we have selected hexatriacontane ($C_{36}H_{74}$:abbreviated to C36) as our focusing substance of investigations.

Two different types of C36 specimens, single crystals and bulk samples, are mainly used in our experiments [2-6]. In the sections 6.3, we use the single crystal of C36 prepared by a dilute solution of xylene. The single crystal is heated in the DSC apparatus up to the definite transition temperature [3,4]. Then the sample is cooled down and measured crystalline structures by WAXS at room temperature. We also show the results of the simultaneous measurement by DSC and time resolved X-ray diffraction using a synchrotron radiation [5].

In the section 6.4, the transitions of the bulk C36 is observed by TSC. We have discussed the TSC method in the chapter 5. The *in-situ* phenomena are studied by the melt-solid interface observed by the TSC apparatus [2]. In the section 6.5, onset mechanism of the transition is discussed by WAXS, SAXS, DSC and polarized optical microscopy [6]. The results of the phase transition of C36 are summarized in the section 6.6.

6.2 Molecule and Phases of C36

C36 is an even alkane (paraffin) with the molecular length equal to 47.5 Å. Phase transitions and structural studies of C36 were developed by the various observations including X-ray diffraction method [7-16]. The melting temperature, T_m, is fixed at 76 °C, which is slightly deviated depending on the purity. While heating from room temperature to T_m, the single crystal of C36 exhibits several phases including a rotator phase before the melt state. We define each phase with a symbol. For simplicity, we introduce here the abbreviated phase notations with the subscripts M_L: low temperature crystalline phase, M_H: high temperature crystalline phase, R: rotator phase and L: melt phase.

At room temperature, the solution-grown single crystals prepared from pure C36 reveal

the M_L (monoclinic) form. When C36 crystal is heated from the room temperature, the M_H phase is observed in the range of 70-73 °C. Then, at 73-75 °C, the M_H form changes to the R phase, which finally goes into the L state at 76 °C. Thus, C36 single crystals exhibit three phase transitions, which are called the solid-solid ($M_L{\rightarrow}M_H$), the solid-rotator ($M_H{\rightarrow}R$) and the rotator-melt ($R{\rightarrow}L$) transitions. During the DSC measurement, the transition temperatures are slightly shifted depending on the purity and amount of the sample.

The crystalline forms of M_L and M_H have been determined in the previous observations [10,11]. The long hydrocarbon molecules are packed in a subcell structure, having the same structure of PE. The known crystal structure of M_L, M_H and PE are compared in Table 6.1. The molecular chains are inclined in the bc-plane in M_L, whereas they are tilted in the ac-plane in M_H. In the present chapter, we explain morphological change during the phase transitions. Based on the results of our investigation, we propose a new $M_L{\rightarrow}M_H$ mechanism in the section 6.3. The new crystalline forms of M_H and R are analyzed in the section 6.4.

Table 6.1   Lattice constants of M_L and M_H crystal [10,11].

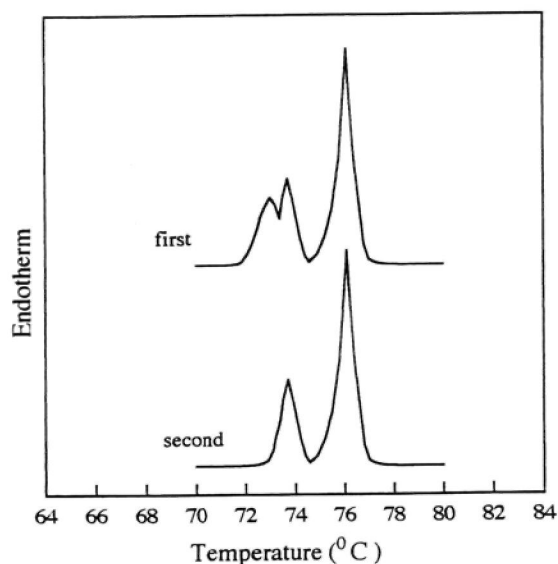| Phase	a (Å)	b (Å)	c (Å)	α (°)	β (°)	γ (°)	Temp. (°C)
M_L	7.42	5.57	48.35	119.1	90	90	20
M_H	7.76	4.90	48.27	90	106	90	20
PE	7.42	4.96	2.534	90	90	90	20

Fig.6.1   DSC thermograms of C36 single crystal obtained by heating rate of 1 °C/min.[4]

6.3 $M_L{\rightarrow}M_H$ Transition of C36 Single Crystal

6.3.1   Thermal measurements by DSC

We used a solution-grown single crystal of C36 for thermal analysis by DSC. The single crystal has a flat shape with 0.1 mm in thickness and 1~2 mm in width and length. Some of

them are observed by lozenge shaped crystals. The DSC thermogram of a solution-grown single crystal with endotherm versus temperature is shown in Fig 6.1. In the first run from room temperature to 80 °C, three peaks appear corresponding to the solid-solid, solid-rotator and rotator-melt transitions. After the first run, the sample is cooled down to room temperature and heated up again in the second run. Due to irreversible phenomena, the $M_L{\rightarrow}M_H$ transition is disappeared in the second run.

In order to observe lamellar structures of C36, we prepared a thick mat, where the several tens of single crystals are piled up on the flat surface. In Fig. 6.2, the WAXS patterns were investigated during heating of the mat. The mat is sandwiched between the heaters. The incident X-rays are parallel to the mat surface. The meridional reflections indicate that the crystalline c*-axis is perpendicular to the flat surface of the mat. In Fig.6.2 (a), the mat is heated to 69°C below the transition temperature. From the meridional reflection, the spacing has been measured to 42.3 Å, corresponding to the lamellar thickness calculated by c sinα of the M_L crystal. After heating to the transition temperature, the spacing of the meridional peaks in Fig. 6.2(c) indicate 46.4 Å, showing good agreement with the calculated value by c sinβ in the M_H form. In the intermediate state, the two layers are coexisted in the meridional reflections in Fig.6.2(b).

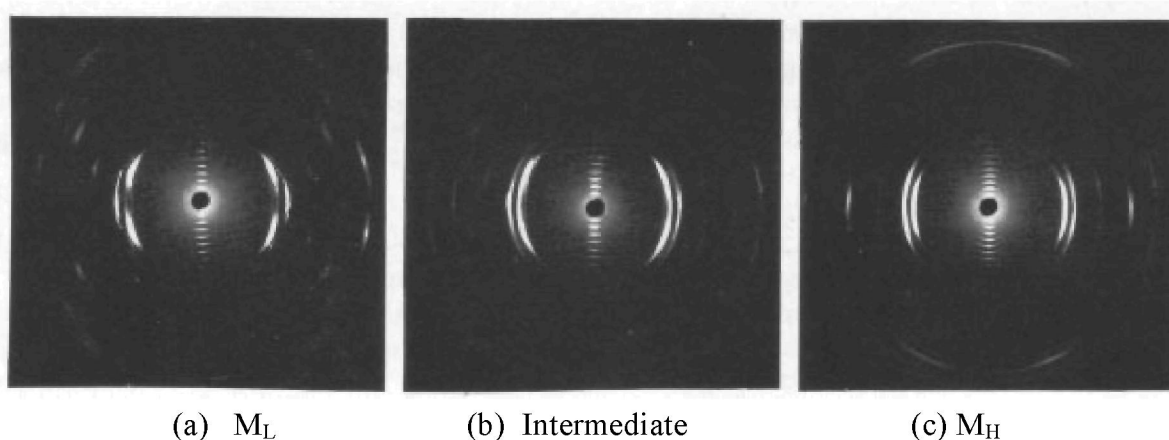| (a) M_L | (b) Intermediate | (c) M_H |

Fig.6.2   WAXS patterns of the single crystal mat during heating of the solid-solid
transition [3].

6.3.2   Basic investigation of the $M_L{\rightarrow}M_H$ transition

The $M_L{\rightarrow}M_H$ transition of C36 has been reported by Schaerer et al., Sullivan, Templin and Takamizawa et al.[13-16]. The precise observation of the transition mechanisms including the solid-solid transition of C33 has reported by Strobl et al.[17]. The above results confirm that the $M_L{\rightarrow}M_H$ transition of C36 is irreversible, accompanied by the shift of the layer thickness. However, it is not clear why M_H is stable above the transition temperature and why the solid-solid transition is irreversible. The known structures of M_L and M_H are compared in Fig.6.3.
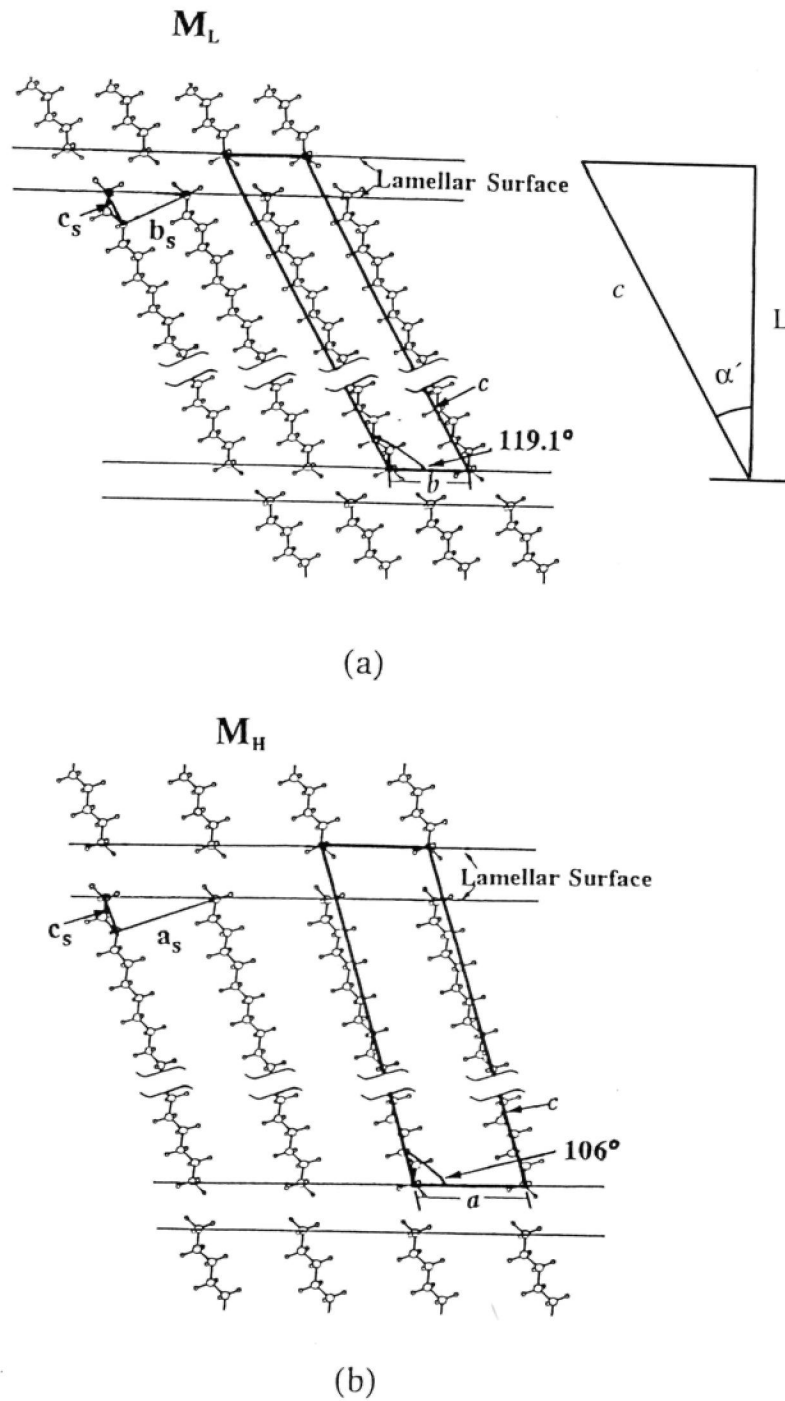
M$_L$

Lamellar Surface

119.1°

(a)

M$_H$

Lamellar Surface

106°

(b)

Fig.6.3   Lamellar structure and molecular packing of the (a) M$_L$ and (b) M$_H$
crystals. a$_s$, b$_s$ and c$_s$ are the subcell structure same as the structure of
PE.   In the M$_L$ structure, the inclination angle of the crystalline
molecule, α', is slightly smaller than α [4].

6.3.3   DSC and X-ray diffraction studies by the step-wise heating

The C36 single-crystal was step-wisely heated by the DSC apparatus. The annealing
procedures are shown in Fig. 6.4. In the first run, the sample was heated up to 72.4°C, and

then cooled down to room temperature (25 °C) for X-ray diffraction measurements. Then in the second run, the same sample was heated to 72.5 °C. In order to explain mixed reflections during the $M_L \rightarrow M_H$ transition, we refer to $(hkl)_L$ and $(hkl)_H$ as the reflection planes of the M_L and M_H phase, respectively.
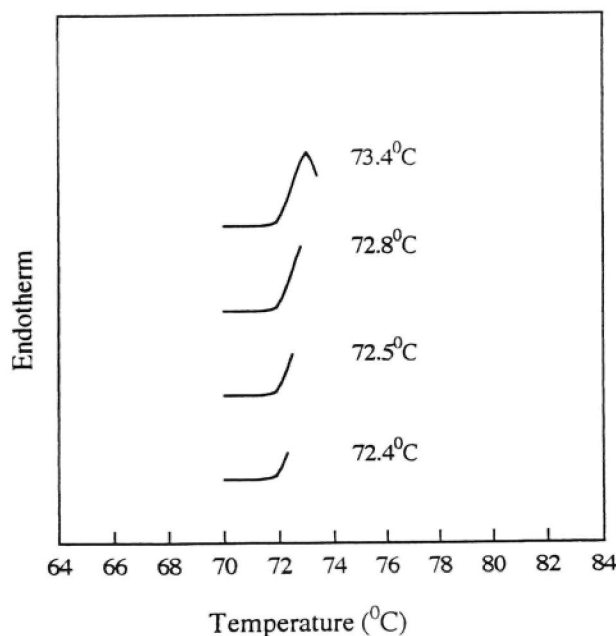

Fig.6.4   DSC thermograms of the partial heat treatment
of the C36 single crystal for X-ray studies [4].

Figure 6.5(a) shows the WAXS pattern of the original crystal before the heat treatment. The diffuse ring arises from thin membrane of amorphous poly(ethylene terephthalate) (PET), which was used for protection of the very thin single crystal from fracture during the experiments. The innermost sharp reflection arises from the $(112)_L$ plane. A weak $(203)_L$ and a sharp $(210)_L$ reflections appear on the diffuse ring along the equator and outside the ring, respectively. Other reflections on the pattern emerge from the symmetry planes of the M_L crystal.

Figures 6.5(b)-(e) denote the WAXS patterns when the crystal was heated to 72.4, 72.5, 72.7 and 73.4 °C, respectively. In Fig. 6.5(b), most of the reflections are similar to those in Fig. 6.5(a), showing most of the crystal remain unchanged. However, some weak reflections appear at a distance greater than the spacing of the $(112)_L$ plane and smaller than that of the $(203)_L$ plane, indicating that the transition is initiated at the most probable region. The new reflections are due to the $(110)_H$ plane with a spacing of 3.69 Å. It is noteworthy that the $(110)_H$ reflections, which appear up and down at 12° deviation from the equator in Fig. 6.5(b), can not be explained by the original orientation of the M_L crystal.

In Fig. 6.5(c), original reflections disappear, and the innermost diffraction peaks that emerge along the circular ring are $(110)_H$ reflections, indicating that the transition takes place in the whole region. The $(200)_H$ reflections appear both on and outside the equator. The appearance of $(200)_H$ reflections just on the equator suggests that the molecules keep the

crystalline axis unchanged during the transition. Furthermore, a new pair of $(200)_H$ reflections, located outside the equator, makes an angle 67° with the equator. This result demonstrates that the molecules are aligned by a new crystalline axis in the transition.

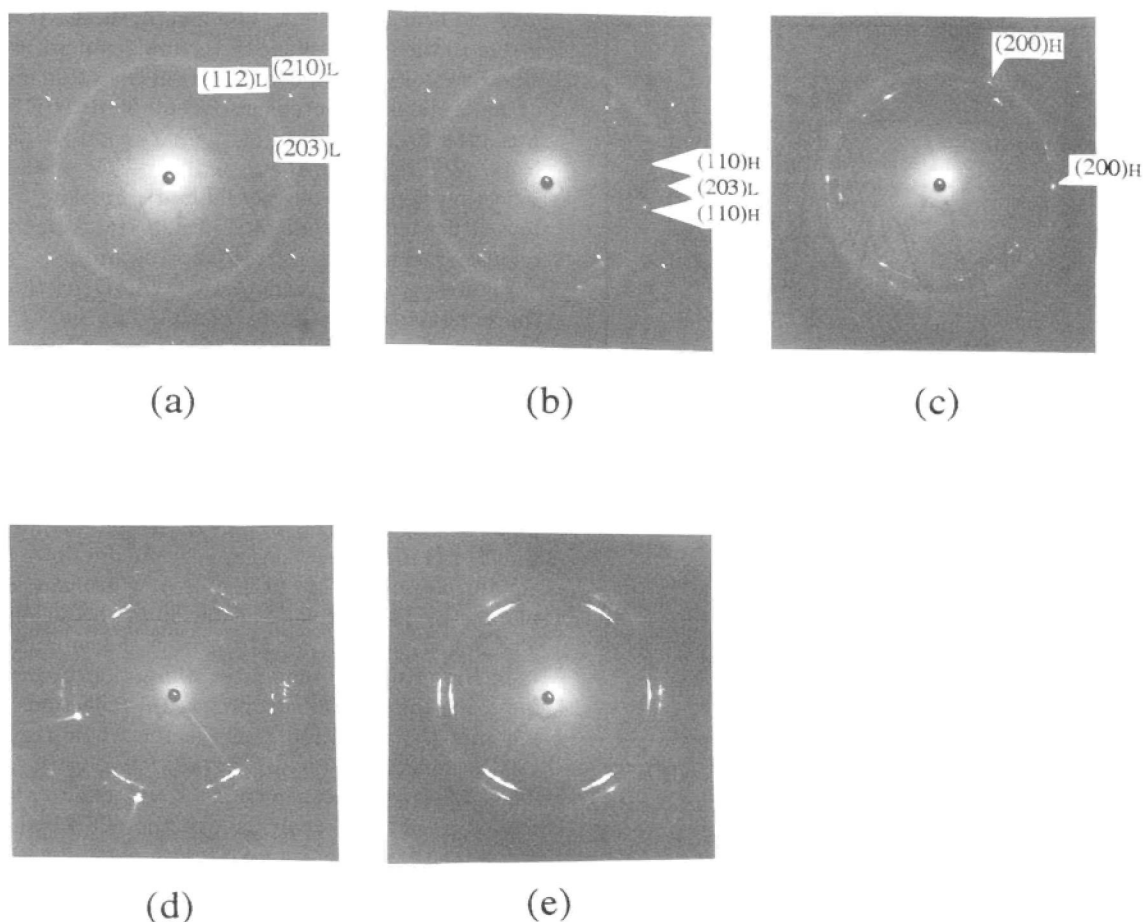Fig.6.5   WAXS patterns taken at room temperature: (a) original single crystal, heated at (b) 72.4 °C, (c) 72.5 °C, (d) 72.7 °C and (e) 73.4 °C. The X-ray beam was put perpendicular to the flat crystal [4].

In Fig. 6.5(d), the reflections are distributed on arcs, showing that the single crystal changes to polycrystallites after the transition. Figure 6.5 (e) shows six broad arcs for $(110)_H$ and also six arcs for $(200)_H$. The arc like reflections indicate that, at a higher temperature after the solid-solid transition, the regularity of the single crystal is destroyed and the original single crystal is fractured into polycrystallites.

6.3.4   Twinned mechanism of the $M_L \rightarrow M_H$ transition

WAXS patterns indicate two different outstanding features in the $M_L \rightarrow M_H$ transition: (i) the $(110)_H$ reflections located up and down the equator (12°) are related to the $(200)_H$ reflections situated outside the equator, and (ii) the $(200)_H$ reflections appear just on the equator. The former one indicates the appearance of a new crystalline a_H-axis at an angle 67° from the equator. The latter one indicates that the M_H crystal keeps the a_H-axis unchanged with the original a_L-axis.
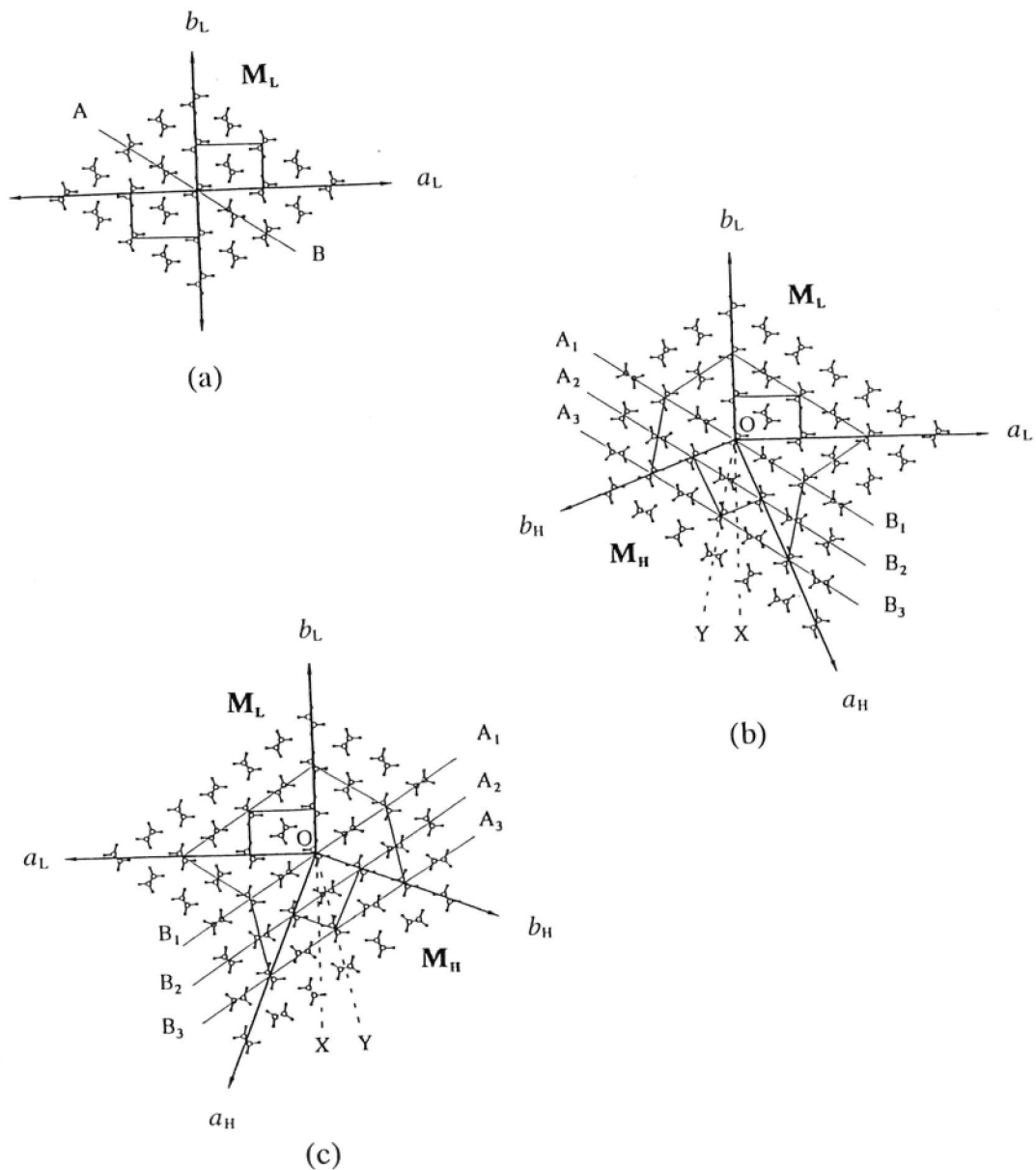
Fig.6.6   Schematic drawing of the projection of plane zigzag chains on the $a_s b_s$-plane of the subcells. The crystalline axes a_L, b_L and a_H, b_H distinguish the M_L and M_H states. (a) The M_L crystal (b) The twin crystals, where transition occurs across the (110) twin plane such as $A_1 B_1$ accompanying new crystalline axes a_H and b_H. (c) The symmetry case of (b) [4].

To find the origin of the new a_H-axis, a mechanism for the formation of twin-crystals can be proposed. Normally, twins are composed of two equivalent individual crystals which share a part of the direction, i.e. at least one crystal plane of the individual crystals must be shared. The transition process from the M_L state to M_H state is analyzed considering the nature of molecular movements during the heat treatment.

Figure 6.6(a) is a scheme, illustrating the projection of the plane zigzag chains of the M_L crystal on the $a_s b_s$-plane of the orthorhombic subcell structure. For convenience of

explanation and analysis of the results, lattice parameters a_L, b_L and a_H, b_H are introduced to distinguish the M_L and M_H phases, respectively. Our experimental results show a possible twinning along the (110) plane, and we point out the structural changes started on this plane i.e. AB plane of Fig. 6.6(a). If the crystal is twinned along this plane, then displacement of molecules involves a shear movement along to A_1B_1, A_2B_2, A_3B_3, as shown in Fig. 6.6(b). As a result, new crystalline axes a_H, b_H of the M_H are grown by the twinning.

In Fig.6.6 (b), the angle, $\angle XOY$, between OX and OY becomes 12°, which is exactly the same as that between the normals of the $(200)_L$ and $(110)_H$ planes. Comparing the WAXS result in Fig.6.5(b), the angular deviation of 12° of $(110)_H$ reflection from the equator shows an excellent fit to the above calculated value. The deviation of 67° for $(200)_H$ reflection from the equator is the same as the angle $(\angle a_L O a_H)$ between the original a_L-axis and the new a_H- axis.

It is noteworthy that, due to the crystal symmetry in the M_L state, there is equal probability for the molecules to have differently oriented twin boundary [Fig. 6.6(c)], generating the different a_H-axis. Due to the twin mechanism, the uniform structure of the original single crystal includes lattice defects, resulting in the observed irreversibility behavior in the DSC thermogram. Due to the formation of the polycrystallites, the a_H-axis is widely distributed as shown by the arcs of Fig. 6.5(e).

The twinned mechanism has an advantage in changing the inclination of molecules from the $(010)_L$ plane to the $(100)_H$ plane of the twinned crystal. The original chain inclination in the $b_L c_L$-plane of the M_L crystal can easily change their inclination in the $a_H c_H$- plane of the M_H crystal by an rotating angle of either +23° or –23° (the angle between b_L and twinned a_H-axis).

On the other hand, the twinning induces positional shifting of the molecules. As shown in Fig. 6.6 (b) and (c), the original M_L molecules are moved by the $M_L \rightarrow M_H$ twinning. The molecular displacement will increase proportional to the twinned region. Due to the disadvantage of the twinning mechanism, the twinned region is restricted in a local area.

6.3.5 Stand-up mechanism of the $M_L \rightarrow M_H$ transition

In Fig.6.5, the WAXS results indicate that the a_H-axis remains unchanged with the original a_L-axis [3]. In this mechanism, the molecules, which incline in the $b_L c_L$-plane of M_L phase, once stand up perpendicular to the lamellar surface producing the Orthorhombic (O) state and then re-incline in the $a_H c_H$-plane of the M_H phase (see Fig. 6.7). This process of transition is called a stand-up mechanism and is denoted here to $M_L \rightarrow O \rightarrow M_H$. The stand-up mechanism requires the molecules for cooperative arrangement to become perpendicular to the lamellar surface and then re-incline into the ac-plane.

Apparently, the M_L crystal is transformed into the M_H crystal by the two possible processes viz. twin-formation and stand-up mechanisms. But, it is not clear which of the two processes takes place earlier and whether there is any correlation between them. Considering that the phase transition is a dynamic process, we require performing a real-time measurements using suitable facility in order to understand the transition mechanism in detail.
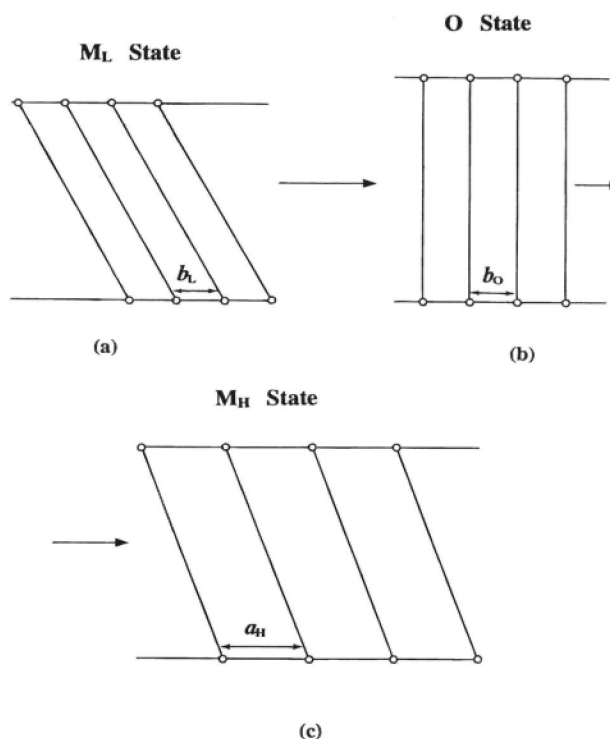
Fig.6.7   Stand-up mechanism: (a) M_L, (b) O and (c) M_H phase [5].

6.3.6 Simultaneous measurements of DSC and X-ray diffraction

For X-ray diffraction, we used synchrotron radiation of wavelength, λ =1.506 Å. For simultaneous DSC and SAXS measurements, we used a PSPC to collect time-resolved X-ray diffraction data. A 2-mm-diameter hole was made in the DSC apparatus to pass the X-ray beam. Figure 6.8(a) shows a DSC thermogram of the sample during heating to 77 °C with a rate of 1 °C /min. For the SAXS measurement, we used a thick C36 mat, piled up several single crystals. This condition produce broadening of the DSC curve as compared with our previous thermogram observed in the single crystal.

The SAXS results during the process of the solid-solid phase transition obtained at temperatures marked in Fig. 6.8(a) are shown in Fig. 6.8(b). At room temperature, only one peak appears at 2θ = 2.03°, which corresponds to the reflection from the $(001)_L$ plane of the M_L crystal. When the measurement is taken at 72.00 °C, two peaks appear at 2θ = 2.03 and 1.81°. The high-intensity peak is from the $(001)_L$ plane of the M_L state having a lamellar thickness of L_L = 42.5 Å, whereas the smaller peak that appears at the lower angle indicates a reflection from the $(001)_O$ plane of the O state, which has a layer spacing of L_O = 47.6 Å. This indicates that lamellar thickening occurs as a result of the $M_L \rightarrow O$ transition. Increasing the temperature, the intensity of the $(001)_L$ peak decreases linearly with the increase of the $(001)_O$ peak.
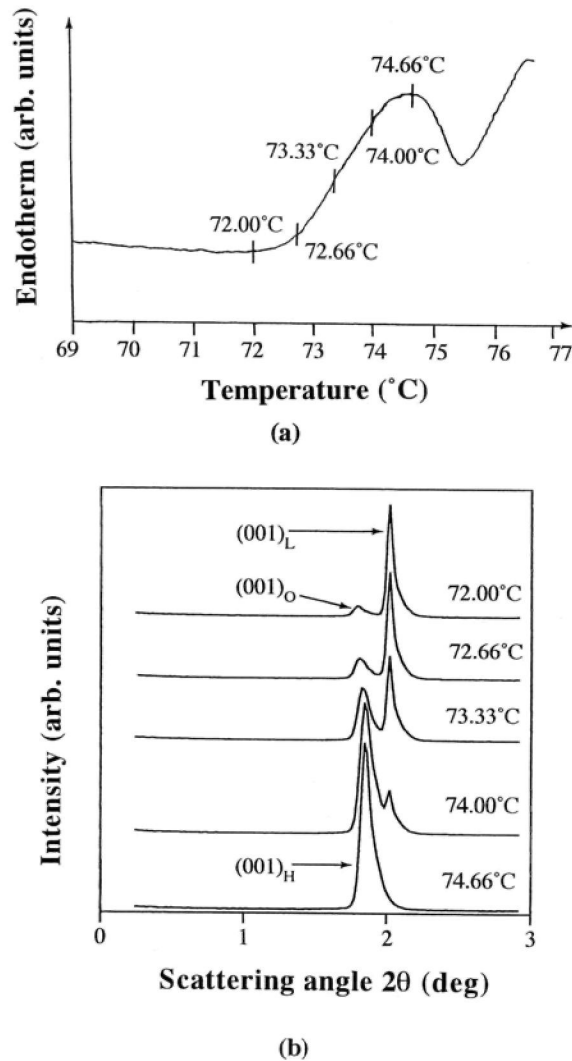
Fig.6.8   Simultaneous measurements of the solid-solid phase transition, (a) DSC thermogram and (b) time-resolved SAXS measurements by PSPC [5].

Further enhancement of the temperature from 73.33 to 74.00 °C shows a shifting of the lower-angle peak to a higher angle. Finally, at 74.66 °C, only one peak appears at $2\theta=1.85°$ in between $(001)_L$ and $(001)_O$ with a spacing of 46.7 Å. This peak corresponds to the $(001)_H$ plane of the M_H crystal. The SAXS results observed here strongly indicate that the transition proceeds as $M_L \rightarrow O \rightarrow M_H$. However, it is difficult to distinguish the effect of the twinned mechanism by the simultaneous SAXS measurement.

6.4 Phase Transition Studies of Bulk C36 by TSC

6.4.1 Experimental conditions

The TSC apparatus used to study phase transitions of C36 are shown in Fig. 5.3b (see chapter 5). Bulk materials of C36 were pre-melted and put in a glass capillary, whose diameter is 1.5 ~ 2 mm. In the TSC, the heater temperature was controlled to 100 °C, which

is 25 °C higher than the melting temperature of C36, and the cooler was cooled by water to 20 °C. The average temperature gradient was about 30 °C/mm due to the narrow distance between the heater and the cooler. The crystallization was started when the sample capillary was moved towards the cooler by a speed of 2 mm/hr. The crystallizing direction was parallel to the z-axis, which was also parallel to the sample capillary. The *in-situ* WAXS measurements were performed on the melt-solid interface. The diameter of the incident X-ray beam was 100 μm.

6.4.2 Appearance of the oriented rotator phase

In a series of the TSC experiments, the incident X-ray beam was passed through a well oriented region near the crystallizing plane. We consider that the structure just below the T_m is the rotator phase. In Fig. 6.9, two reflections appear up and down from the equator, and a set of parallel reflections are aligned on the meridian near the direct beam. The equatorial reflection corresponds to a spacing of 4. 321 Å, and the two reflections, up and down from the equator, showing the same distance have a spacing of 4.17 Å. The meridional reflections show existence of a layer structure in the rotator state having the spacing of 46.0 Å. The meridional reflection corresponds to the (001) plane, indicating that the c^*-axis is parallel to the Z-axis.
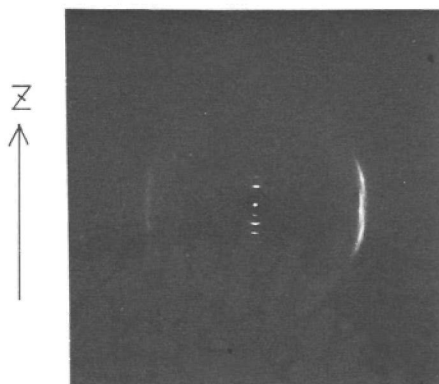

Fig.6.9   X-ray diffraction pattern of the oriented rotator phase [2].

Most of the paraffins are crystallized through the rotator phase near their melting temperatures. Piesczek *et al.* [17] have shown that the rotator phase of C33 (tritriacontane) indicates a multiple twin structure of triclinic form where the chain axis is tilted from the end group planes, and the lateral packing of molecules closely approaches to the hexagonal form [19].

Based on the X-ray pattern of C36, it is possible to analyze the reciprocal lattice of the rotator phase as shown in Fig. 6.10, where the filled circles represent the reciprocal lattice of one crystal. The multiple reciprocal lattices indicate that the crystal is a multiple twin structure. The reciprocal lattice shows that the molecule is tilted by 17° from the c^*-axis. The tilting occurs in the (010) plane and the resulting crystalline form is monoclinic. In this form, the molecule is tilted nearly the same way as that found in the triclinic structure of C33 [17], although the tilt direction is a little different.
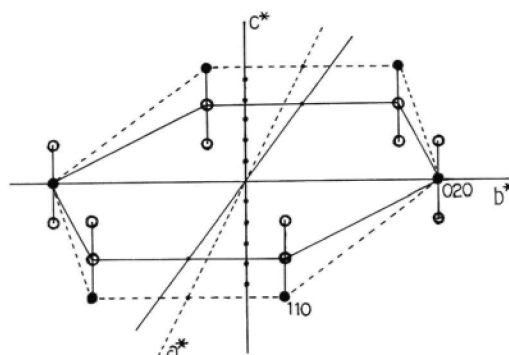
82

Fig.6.10   The reciprocal lattice of the rotator phase. The crystal has multiple twins. The reflections from one crystal are shown by filled circles [2].

From the reciprocal lattice, the lattice constants of the rotator crystal is determined as a = 4.98 ± 0.02 Å, b = 8.62 ± 0.03 Å, c = 48.10 ± 0.15 Å, β=107.0 ± 0.5° (or 73.0 ± 0.5°), $\alpha = \gamma$ = 90°. The indices of the inner and the outer reflections are 020 and 110, respectively.

Though the molecules are inclined in the lamellae, the R molecules along the c-axis are packed in hexagonal with rotating symmetry around the c-axis. During the L→R transition in the melt crystallization, it is possible to consider nematic or smectic state before the R phase. Appearance of the molecular orientation in the L→R transition is observed in TSC (See section 5.4.3, pp60).

6.4.3 Oriented crystalline form of bulk C36

The bulk C36 sample was crystallized by TSC and cooled to the room temperature. Figure 6.11 shows the WAXS pattern of the well-oriented C36 crystal. The meridional reflections confirm that the crystal has the lamellar structure, whose normal is parallel to the Z-axis. The crystalline (001) plane has a spacing of 46.4 Å. Some equatorial reflections are largely split from the equator. The observed spacing and tilt angles of the WAXS reflections are listed in the right rows of Table 6.2. From the known structures of M_L and M_H, values of d_{cal} and spilt angle are also calculated as listed in Table 6.2. The observed values show well fitting to those of the M_H phases.

Based on the observed spacing and split angles, we determine new crystalline constants of the monoclinic phase. In Table 6.2, we confirmed this form as M_H, because the monoclinic crystal is the same as that observed in the high temperature form by the single crystal (see in the section 6.3.4). The indices of the second and the fourth equatorial reflections (Fig. 6.11) are assigned as 200 and 020, respectively. We finally evaluate the cell parameters of M_H: a = 7.76 ± 0.07Å, b = 4.90 ± 0.02 Å, c = 48.27 ± 0.45 Å, β= 106.0 ± 2.0°, $\alpha = \gamma$ = 90°. The spacings and split angles of the c^*-oriented M_H crystal are listed in Table 6.2. These values well coincide with the observed ones. The M_H phase is similar to the high-temperature monoclinic form observed by Sullivan and Weeks [15], and Takamizawa et al. [18] in the heating process of solution-grown C36 single crystal.
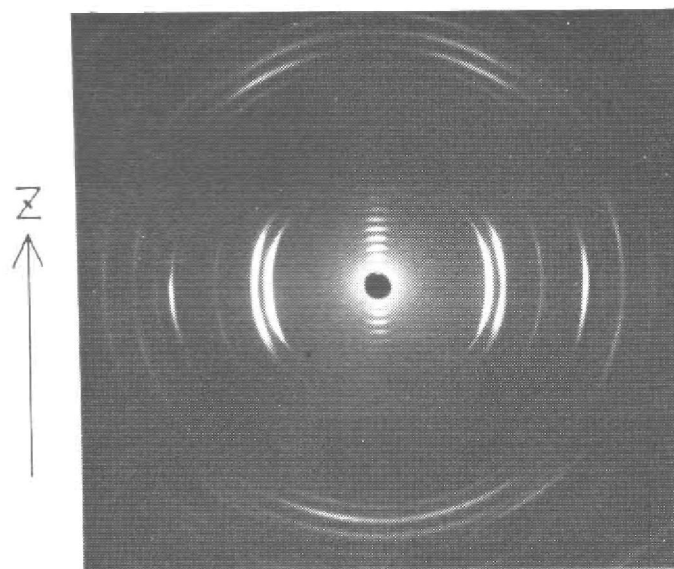
Fig.6.11 WAXS pattern of the melt-grown crystal by TSC (at 20°C) [2].

Table 6.2 Spacings and split angles from the equator observed in Fig. 6.11, and calculated values of M_L and M_H phases

M_L Phase			M_H Phase			Observed	
hkl	d_{cal} (Å)	Split angle (°)	*hkl*	d_{cal} (Å)	Split angle (°)	d_{obs} (Å)	Split angle (°)
110	4.07	24.0	110	4.10	8.7	4.11	9.0
020	3.71	0	200	3.73	16.0	3.73	16.0
120	2.95	17.1	210	2.97	12.7	2.95	11.5
200	2.43	29.1	020	2.45	0	2.45	0
210	2.31	27.5	120	2.33	4.9	2.33	4.0
130	2.20	12.7	310	2.22	14.2	2.20	13.0
220	2.03	24.0	220	2.05	8.7	2.04	9.0
001	42.25	-	001	46.4	-	46.4	-

The M_L and M_H phases consist of the orthorhombic subcell shown in Fig. 6.3. In the M_L cell, the neighboring molecules are displaced by one-zigzag period (2.54 Å) in the bc-plane [12]. Considering the displacement in the ac-plane, we can estimate the inclination angle, ψ, of the M_H phase. Then,the value of ψ is calculated to be: $\psi = \tan^{-1}(2.54/d_{100})$ $= \tan^{-1}(2.54/7.46) = 18.80°$. The discrepancy between this value and the observed one (16.0°) is about 3°. Accordingly, the molecular axis is considered to have further tilted from the crystalline *c*-axis.

6.4.4 Mechanism of R→M_H transition

Figure 6.12 represents the WAXS patterns taken after exposing the X-ray beam at different positions near the melt-solid boundary. As the incident X-ray moves from the boundary to downwards at 200 and 400 μ, two equatorial reflections of Fig.6.12a change to four (Fig.6.7b) and then to three reflections (Fig.6.12c). The arcs, labeled as 1 and 2 in Fig.6.12a, are 020 and 110 reflections of the rotator crystal, respectively. In Fig.6.12b, the position of 1 approaches to that of 2, which shows that the spacing of the (020) plane decreases. Besides, the intensity of these two reflections decreases as the transition proceeds and almost disappears in Fig. 6.12c, whereas the intensity of other three reflections (labeled as 3, 4 and 5) increases.

In Fig.6.12c, weak reflections other than the 3, 4 and 5 are recognized at the higher angles. The spacings and the split angles measured from the equatorial reflections nearly match to those of the M_H phase. The observed values indicate the monoclinic crystal having lattice constants of a = 8.13 ± 0.07Å, b = 5.00 ± 0.02 Å, c = 48.50 ± 0.45 Å, β= 107.0 ± 2.0°, α = γ = 90°. Considering the temperature gradient of 30 °C/mm, the temperature of the crystal was 63 °C. Due to the thermal expansion, values of the M_H crystal are slightly different from the crystal observed at room temperature. The above results are summarized in Table 6.3.

Table 6.3 Lattice constants and crystallographic orientations of C36 crystal [2, 3, 10, 11].

Phase	a (Å)	b (Å)	c (Å)	α (°)	β (°)	γ (°)	Temp. (°C)
M_H	7.76	4.90	48.27	90	106	90	20
M_H	8.13	5.00	48.50	90	107	90	63
R	4.98	8.62	48.10	90	107	90	75

Comparing the rotator crystal observed by Fig.6.9 and the M_H in Fig.6.12c, the transition from R to M_H phase requires a contraction of the inter-molecular distance in the direction normal to the rotator (110) plane, which is parallel to the a_H-axis with the contraction of a_H-axis by 0.5 Å. Thus, the solid-solid transition from the R phase to the M_H phase occurs by 30° rotation of the tilt direction as well as by 0.5 Å anisotropic contraction of the intermolecular distance. After cooling the sample to room temperature, the M_H form undergoes further thermal contraction to 0.37 and 0.10 Å in the direction of a_H- and b_H-axis, respectively.
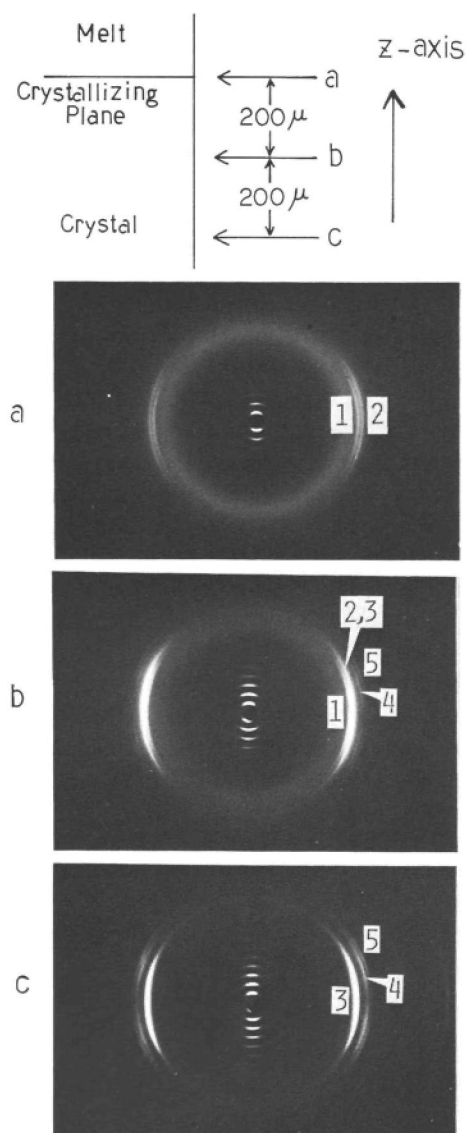
Fig.6.12   WAXS patterns of the crystallizing region. The center of the incident
            X-ray beam is (a) just on the crystallizing plane and (b) 200 μ,
            (c) 400 μ downwards from it [2].

6.5   Onset Mechanism of the Phase Transitions

6.5.1 Molecular motion during the $M_L \rightarrow M_H$ transition

In order to explain the motivation of the solid-solid transition, the surface structure of lamellae of the M_L and M_H phases is compared. Figures 6.13 shows side-views of the *bc*- and *ac*-plane, respectively. In each case, the thick and the thin molecules are located at the corners and at the central position of the unit cell. Though the sub-cell structure is same as polyethylene, packing difference appears on the lamellar surface. In case of the M_L state, the CH_3 groups is aligned in the same direction producing a smooth surface, whereas the packing in the M_H crystal is anti-symmetrical producing a rough surface.
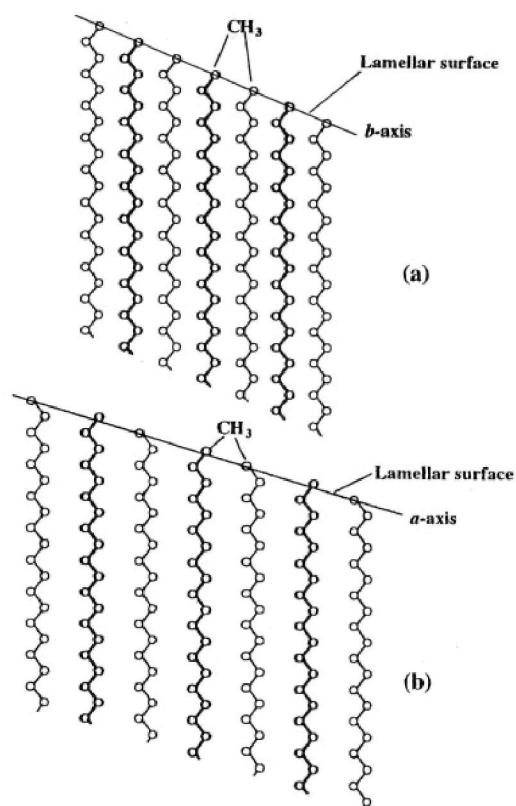
Fig.6.13   Side-views of molecules on (a) the bc-plane of the M_L phase showing smooth lamellar surface and (b) the ac-plane of the M_H phase showing a rough surface of the lamella.

The molecular motion in the lamellar structure first occurs along the chain direction. Initial movement of the hydrocarbon molecules is known to the flip-flop motion by which the molecules rotate 180° together with a longitudinal motion along the chain direction. Considering the packing of the CH_3 terminal, the rough surface of the M_H phase is suited to start the flip-flop motion. Thus, the $M_L \rightarrow M_H$ transition occurs related to the roughness of the surface structure.

The above discussion indicates that surface roughness controls the solid-solid phase transition. To confirm the effect, impurity molecules of the shorter length than C36 were used to produce a rough surface.

6.5.2 Effect of impurity on the transition
(i)   Thermal investigation by DSC

The length of n-dotriacontane (C32) molecule is smaller than that of C36. Therefore, we introduced C32 as the impurity. At first, we prepared two kinds of p-xylene solutions having concentration $S_C = 0.1$ and 0.2 wt%. With the known amount of solute, the impurity fraction is calculated by $I_F = [C32/(C32+C36)]$. In order to examine the effect, we prepared 6 solutions (A, B, C, D, E and F) as listed in Table 6.4. The single crystals were prepared below 10 °C in the refrigerator.

Table 6.4 Sample preparation with different S_C and I_F

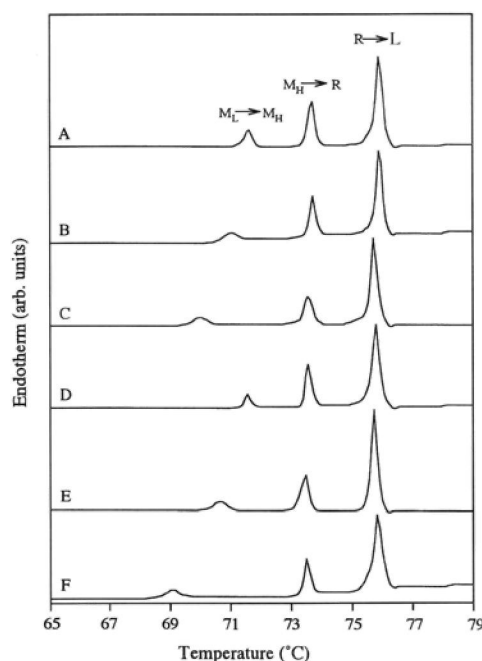| Samples	(S_C wt%)	I_F (%)
A	0.1	0
B	0.1	0.5
C	0.1	1.0
D	0.2	0
E	0.2	0.5
F	0.2	1.0

Fig.6.14   DSC thermograms of samples A–F [6].

DSC thermograms exhibit three endothermic peaks corresponding to the $M_L{\rightarrow}M_H$, $M_H{\rightarrow}R$ and $R{\rightarrow}L$ transitions as in Fig. 6.14. The peak-temperatures are shifted depending on S_C and I_F. The DSC results also show that the $M_L{\rightarrow}M_H$ transition peaks become wider when the impurity concentration increases.

The peak-temperature as a function of impurity concentration is plotted in Fig. 6.15. The clear circle corresponds to the values for the series of the samples A–C (S_C = 0.1 wt%) and the filled circle denotes the variation for another series D–F (S_C = 0.2 wt%). It is obvious from the graph that the $M_L{\rightarrow}M_H$ transition is shifted towards a lower temperature, depending not only on I_F but also on S_C, because the case of S_C = 0.2 wt% (filled circles) show lower transition temperature than that of S_C =0.1 wt% (clear circles). The pure samples of two different concentrations do not show any significant deviation of the transition temperature, whereas the deviation increases with increasing impurity. The peak-temperature is slightly deviated in the $M_H \rightarrow R$ transition and is almost the same in the $R{\rightarrow}L$ transition.
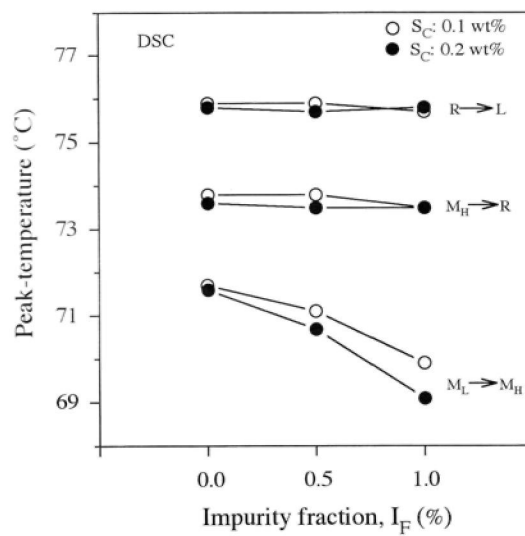
Fig.6.15   The transition temperature as a function of I_F [6].

(ii)   Observation by time-resolved X-ray measurements

Figure 6.16 shows three SAXS patterns taken at room temperature for samples A–C. The peaks of each pattern corresponding to the scattering angle $2\theta = \pm 2.03°$ come from the $(001)_L$ plane of the M_L phase. Another observable difference of the diffraction patterns is a low-angle scattering (ζ-scattering) near the origin. The ζ-scattering intensity increases with increasing sample impurity.

The photograph in Fig. 6.17(a) is taken at room temperature for sample C to observe a two-dimensional pattern of the ζ-scattering. The result shows that the ζ-scattering is located on the meridian. From the steak-like ζ-scattering, we can analyze the existence of a flat-shaped defect in the sample C developed perpendicular to the meridian as illustrated in Fig. 6.17(b). As the $(001)_L$ spacing is the same in the three samples, the defects do not disturb the lamellar periodicity.
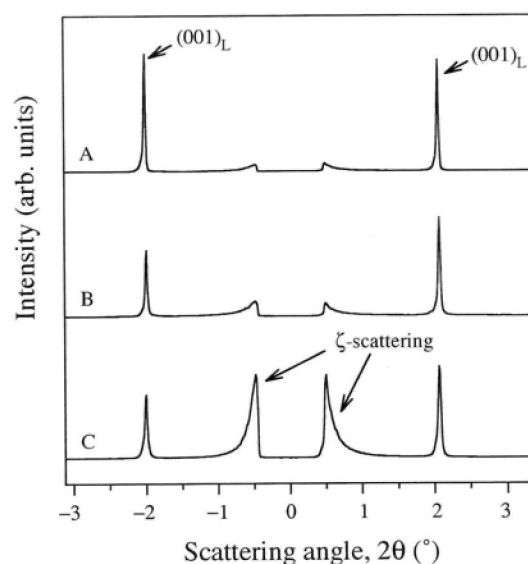

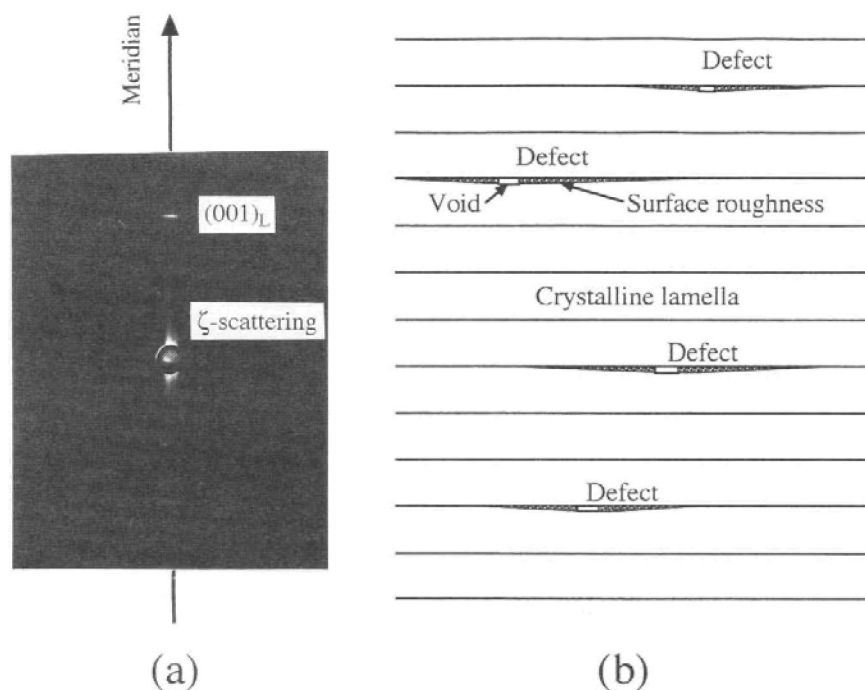Fig.6.16 SAXS results collected by PSPC at room temperature of A–C [6].

Fig.6.17   SAXS photograph of sample C taken at room temperature, (b) Schematic
           model of the crystalline defects developed inside the crystal [6].

Three-dimensional presentations of SAXS data form the series A–C over a temperature range of 69 –75 °C are displayed in Figs. 6.18(a) – (c). The plots consist of X-ray scattering intensity versus reciprocal space, $2\sin\theta/\lambda$, as a function of the temperature: T_1 and T_2 correspond to starting temperatures of the $M_L{\rightarrow}M_H$ and the $M_H{\rightarrow}R$ transitions, respectively.

In case of sample A [Fig. 6.18(a)], the value of T_1 is $\approx$ 72.2 °C. The intensity of the $(001)_L$ peak shows smooth increase before T_1 and the $(001)_H$ peak appears at the inner angle. In the range $T_1{<}T {<}T_2$, the $(001)_L$ and $(001)_H$ peaks coexist until the smooth disappearance of the M_L peak. The M_H state is ultimately transformed into the R state at $T_2 \approx$ 73.4 °C accompanying by a conspicuous reduction in intensity of the $(001)_H$ peak. The intensity of the ζ-scattering is very weak in the sample A.

In case of sample B [Fig. 6.18(b)], the onset of the solid-solid transition is observed when $T_1 \approx$ 71.6 °C. A slight fluctuation of the intensity is observed in the $(001)_L$ peak. Then, the intensity of the M_H state changes from the $M_H \rightarrow$R transition at $T_2 \approx$ 73.4 °C. In addition, the ζ-scattering observed at room temperature [Fig. 6.17 (a)] disappears at T_2.

Sample C [Fig. 6.18(c)] undergoes the $M_L{\rightarrow}M_H$ and the $M_H{\rightarrow}R$ transitions at $T_1 \approx$ 70.7 °C and $T_2 \approx$ 73.2 °C, respectively. The intensity of the M_L state fluctuates considerably during the transition to the M_H state. Then, the intensity shows a sharp decrease during the $M_H \rightarrow$R transition and is unchanged in the R state. The intensified and distributed ζ-scattering falls sharply at T_1 and disappears at T_2.

The three-dimensional presentations of SAXS for the samples D, E and F resemble the previously described results corresponding to A, B and C, except that the values of T_1 and T_2 are slightly lowered.
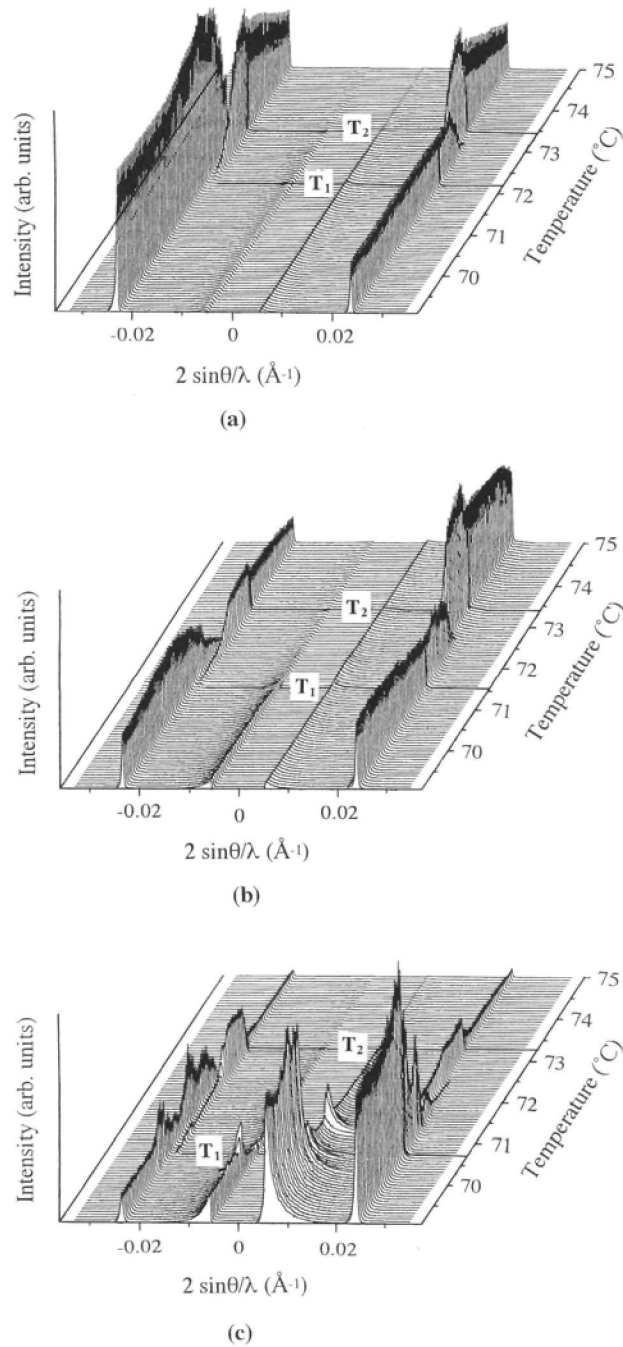
90

Fig.6.18   Three dimensional patterns of the X-ray intensity as a functions of scattering
angle and temperature for samples (a) A, (b) B and (c) C [8].

(iii)   **Comparison of onset temperature**

The starting temperatures T_1 and T_2 observed by DSC and SAXS, respectively, are compared in Fig.6.19. T_1 as observed by SAXS shows the onset of structural change. The SAXS results show T_1 of the structural onset is 1 °C higher than the T_1 observed by DSC (thermal onset) result. This fact strongly suggests that there is a time lag between the starting
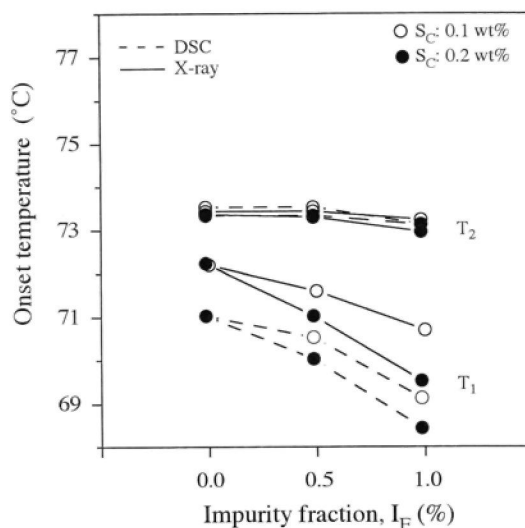
Fig.6.19   Comparison of the onset temperature of transition
as observed by DSC and SAXS [6].

motion of the structural change and the absorption of the thermal energy. The T_2 values are almost identical in both measurements. This fact suggests that the structural change in the $M_H \rightarrow R$ transition appears soon after the absorption of the thermal energy.

(iv)   Observation with polarizing microscope

Fig.6.20 shows the image of a lozenge-shaped pure crystal (sample A) during the intermediate stage of the $M_L \rightarrow M_H$ transition. The long and short diagonals correspond to the crystallographic a_L- and b_L-axes, respectively. The lozenge-edges are the $(110)_L$ planes of the M_L crystal. The phase transition begins from the edge and the tip of the two $(110)_L$ boundaries moves along the b_L-axis as pointed out by arrows. After the $M_L \rightarrow M_H$ transition, the region M_H becomes dark due to the difference of molecular orientation with respect to the M_L state. The movement of the boundary is a macroscopic phenomenon of the $M_L \rightarrow M_H$ transition.

The effect of impurities was also investigated thoroughly for the other samples with the heat treatment following a rate of 1°C/min. Consistent with DSC and X-ray measurements, the transition temperature observed from the boundary movement is lowered with increasing I_F and S_C. However, the boundary resembles in all the samples where the $M_L \rightarrow M_H$ transition commonly starts from the edges of the impure crystals producing transition frontiers parallel to the $(110)_L$ plane.

In the present work, the sample was heated for all three measurement techniques viz., DSC, SAXS and microscopy. During the heat treatment, the measured temperature was considered to be the same as the sample temperature in DSC and SAXS measurements, because the temperature was monitored by a thermocouple placed in the vicinity of the sample which was under complete thermal insulation from the environment. Therefore, the temperatures of DSC and SAXS are subject to a maximum error of 0.25 °C. In Fig.6.19, the T_2 values show a good fit in both measurements. This fact strongly indicates that the 1 °C deviation observed in T_1 is meaningful and highly accurate.
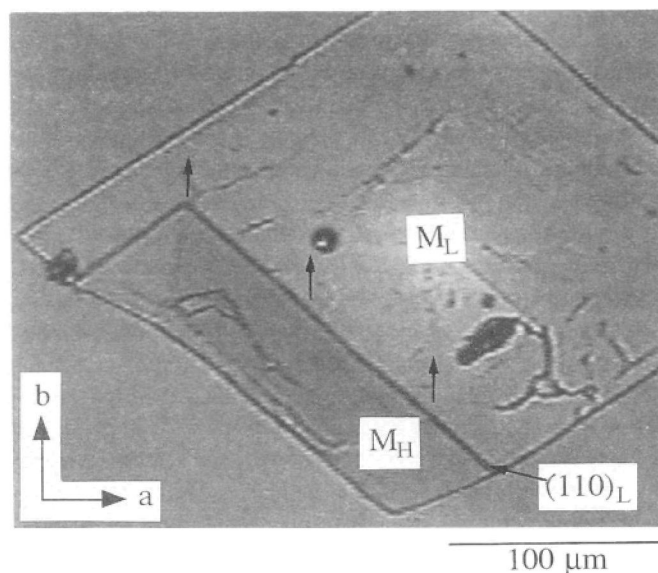
Fig.6.20 An optical image during the solid-solid phase transition of
a lozenge-shaped single crystal of sample A [6].

(v) Defects induced by the impurity

The results in Fig. 6.14 clarify that the solid-solid transition temperature decreases depending on I_F and S_C. I_F must play the leading role and S_C has an additional effect, because there is no temperature reduction in the pure samples crystallized at different S_C (Fig.6.15). In order to explain the decrease of the transition temperature, we first discuss the defects inside the crystal which are the starting (onset) of the transition.

The low-angle streak of Fig. 6.17(a) suggests that sample C contains thin plain-like defects developed perpendicular to the lamellar normal. Considering the average molecular cross section ≈ 18 Å in the crystal, it is difficult for one molecule to form a flat defect. All the samples, except for A and D, were crystallized from a binary mixture of C36 and C32 molecules, where the difference of chain length between these molecules was 5.08 Å. If we consider the gathering (aggregation) of several C32 molecules, then the void spreads in the interlamellar region as shown in Fig. 6.17(b).

We take into account an additional effect due to the S_C during the crystallization, because the solution concentration controls the growth rate resulting in a surface roughness in the lamellar structure at higher concentrations. As the DSC results indicate a strong correlation between I_F and S_C, the roughness must originate from the void of C32. Hence the flat-shaped defects shown in Fig. 6.17(b) are developed by multiple defects of I_F and S_C.

(vi) Onset of the transition from primary nucleation

For the solid-solid transition, the molecular packing of the M_L crystal may control the transition temperature. In a perfect crystal, the thermal vibrations and/or rotations of the molecules are strictly restricted due to the steric hindrance of the identical molecules occupying by the regular lattices. Thus the cooperative motion of molecules for the onset of

the solid-solid transition requires a higher thermal energy. Hence the transition occurs at higher temperature in the pure crystal.

In case of binary crystals, the transition is considered to start from the defect because the molecular movement is less restricted at the periphery of the defects. If we consider the transition nucleus, the number, N, of the nucleus can be assigned as $N = P_o \times N_d$, where P_o and N_d are the initial nucleation-rate (probability) and the number of defects, respectively. N_d normally depends on I_F in the impure sample and appears as spontaneous defects in the pure sample. N_d is also emphasized by S_C as mentioned in the previous discussion. Since the primary nuclei increase with N, the transition starts at lower temperature with increasing I_F and S_C. From these concepts, the results observed by DSC (Fig.6.15) can be consistently explained by nucleation induced from the defects. In the initial stage, the transition must develop in a lateral direction without spreading to the neighboring lamellae (longitudinal direction) .

The polarizing microscopy shows that the solid-solid transition develops on the frontier (Fig.6.20). This finding reveals that the $M_L \rightarrow M_H$ transition proceeds in the bulk region, where a number of lamellae move cooperatively. A crystal of 0.5 mm thickness contains more than 10^4 lamellae where the cooperative transition must propagate in a direction perpendicular to the lamellae. Thus, the bulk transition frontier requires a secondary nucleation developing from the primary nuclei.

In Fig.6.19, values determined by SAXS are always shifting to more than 1°C higher than the values observed by DSC. From this discrepancy, it is clear that the three-dimensional propagation of the solid-solid transition requires a higher energy or time retardation.

The above results can be explained if we define the secondary nucleation with the value of P×N, where P is the bulk nucleation-rate (probability) among the nucleation sites N ($N = P_o \times N_d$). Initially, the transition starts at the nucleation sites N for which the DSC onset-temperature appears depending on the thermal movement of the molecules. In this stage, the solid-solid transition is located around the defects showing no change of lamellar spacing. After a while, the secondary nucleation is grown in the bulk. Then a transition frontier observed by the microscope moves and spreads through the crystal. After growing and passing the frontier, the $(001)_L$ peak changes to the $(001)_H$ peak as observed by SAXS at T_1. Thus, the difference in T_1 values between DSC and SAXS is explained by the time lag for development of the secondary nucleation from the primary nucleation sites.

The most probable position of the secondary nucleation is the edge of the lozenge-shaped single crystal, because the molecules can easily move with less inhibition of the surrounding molecules. As a result, the transition boundary occasionally starts from the edge of the single crystal. During the solid-solid transition, both the primary and secondary nucleation depends on N_d for which the transition temperatures observed by DSC and SAXS and optical microscopy decrease with I_F and S_C.

(*viii*) Change of X-ray intensity and the onset mechanism of other transitions

In the SAXS results of Fig.6.17, the intensity of the ζ-scattering decreases with increasing temperature and the intensity of the $(001)_H$ peak also falls at the $M_H \rightarrow R$ transition. As the molecular movements in the M_H state are enhanced due to high temperature, a decrease of ζ-scattering intensity is obtained by migration of defects with increased

molecular movements. Thereafter, the molecular motions are subjected to further increase in the rotator phase for which the defect structure completely disappears and ζ-scattering is not found in the SAXS patterns. The density difference between the lamellar and interlamellar parts also decreases due to the increase of the molecular motion in the R state from the M_H state and hence the intensity sharply falls in the SAXS results.

In Fig.6.15, the transition temperatures of the $M_H \to R$ and $R \to L$ are not affected by I_F and S_C. In the states of M_H and R, the lamellar surface is more disordered due to enhancement of molecular motions. Accordingly, the transition commences without any time lag as evident from the T_2 values of Fig.6.19. Due to the roughness in the M_H and R structures, the onset of the $M_H \to R$ and $R \to L$ transitions occurs with less dependence on I_F and S_C.

6.6 Concluding Remarks

1. C36 exhibits M_L, M_H, and R phases. The long chain molecules are aligned parallel to each other in the layer. The lattice constants of the phases are confirmed and newly determined in the present research. The crystalline constants are given in Table 6.5, where the value c includes interlayer spacing.

Table 6.5 Lattice constants and crystallographic orientations of C36 crystal [2, 3, 10,11].

Phase	a (Å)	b (Å)	c (Å)	α (°)	β (°)	γ (°)	Temp. (°C)
M_L	7.42	5.57	48.35	119.1	90	90	20
M_H	7.76	4.90	48.27	90	106	90	20
M_H	8.13	5.00	48.50	90	107	90	63
R	4.98	8.62	48.10	90	107	90	75

2. *The solution grown crystal has the M_L form*. Molecules are inclined in the bc-plane by 29.1° composed with the layer. Orders of 10^4 layers are piled up in a single crystal.

3. On the heating process of the M_L single crystal, the molecules are cooperatively moved to the orthorhombic state without inclination, then again inclined in the ac-plane in the $M_L \to M_H$ transition. *The cooperative and simultaneous $M_L \to O \to M_H$ motion is called the stand-up mechanism*.

4. During the $M_L \to M_H$ transition, the single crystal frequently reveals twinning with rotating the crystalline axis by 23°. The *twin-formation* is more advantageous over the stand-up mechanism, because the cooperative motion of molecules during $M_L \to O$ need higher energy. Hence the twinned mechanism occurs at lower temperature than that of the stand-up mechanism. In contrast, the twin formation is accompanied by the expansion of a_L–axis and contraction of b_L –axis. The change in dimension disturbs the crystal growth. The twinned mechanism is then limited to a local effect activated in a small region. This is why no reflection from M_H layers has been observed in the early stage of the transition.

5. During the $M_L \rightarrow M_H$ transition, the single crystal is fractured into poly-crystallites, which causes the *irreversible phenomena in the $M_L \rightarrow M_H$ transition*.

6. Increasing temperatures, the M_L molecules are oscillated by the so-called flip-flop motion with shifting along the chain direction. The surface roughness of the CH_3 terminals in the M_H state has advantage for the movement. Then *$M_L \rightarrow M_H$ transition is controlled by the surface roughness*.

7. Using homologous C32 molecules, the impurity effect confirms the enhancement of $M_L \rightarrow M_H$ at lower temperature. Considering the nucleation of the phase transition, the results of DSC and SAXS are consistently explained: the impurity produces defects at the interlayer. *The onset procedure of the transition is directly affected to the number of the defects*. The transition temperature by DSC is lowered depending on the defects. For the macroscopic transition including 10^4 layers, it is necessary to have a larger defect, taking a retardation time as observed in the SAXS results.

8. For the macroscopic phenomena observed by the polarized microscope, the clear transition domain indicates the macroscopic transition appeared at the edge of the single crystal. As the cooperative motion of the several hundred layers, *the macroscopic transition is mainly proceeded by the stand-up mechanism*.

9. *In the melt-crystallization by TSC, the new crystalline state of the M_H and R phases are determined* as shown in Table 6.5. The L$\rightarrow$R and R$\rightarrow M_H$ transition mechanism is also discussed: Through the possible nematic and/or smectic states, the melt molecules are grown to R. By decreasing the temperature, R$\rightarrow M_H$ occurs by 30° rotation of the tilt direction as well as by 0.5 Å anisotropic contraction of the intermolecular distance. After cooling the sample to room temperature, the M_H form undergoes further thermal contraction to 0.37 and 0.10 Å in the direction of a_H- and b_H-axis, respectively.

References

1. J. C. Anderson, K. D. Leaver, R. D. Rawlings and J. M. Alexander, *Material Science, Fourth Ed.*, Chapman and Hall, New York (1991), (Chap. 12, pp. 361).
2. T. Asano and H. Abe, *J. Phys. Soc. Jpn.*, **53**, 1071 (1984)
3. T. Asano, *J. Phys. Soc. Jpn.*, **54**, 1403 (1985).
4. T. Asano, M. F. Mina and I. Hatta, *J. Phys. Soc. Jpn.*, **65**, 1699 (1996).
5. M. F. Mina, T. Asano, H. Takahashi, I. Hatta, K. Ito and Y. Amemiya, *Jpn. J. Appl. Phys.* **36**, 5616 (1997).
6. M. F. Mina, T. Asano, R. Nuryadi, C. Sawatari, H. Takahashi, I. Hatta, *Jpn. J. Appl. Phys.*, **38**, 164 (1999).

96

7.   A. Muller and K. Lonsdale, *Acta Cryst.* **1**, 129 (1948).

8.   M. G. Broadhurst, *J. Res. Natl. Bur. Stand. Sect.* **A66**, 241, (1962).

9.   S. G. Nyburg and J. A. Potworowski, *Acta Cryst.* **A29**, 347 (1973).

10. H. M. M. Shearer and V. Vand, *Acta Cryst.*, **9**, 379 (1956)

11. P. W. Teare, *Acta. Cryst.*, **12**, 294 (1959).

12. D. C. Basset and A. Keller, Proc. *Eur. Reg. Conf. on Electron Microscopy*, Delft, **1**, 284, (1960)

13. P. K. Sullivan, *J. Res. Natl. Bur. Stand.*, **A78**, 129 (1974)

14. A. A. Schaerer, C. J. Busso, A. E. Smith and L. B. Skinner, *J. Am. Chem. Soc.*, **77**, 2017 (1955)

15. P. R. Templin, *Ind. Eng. Chem.*, **48**, 154 (1956)

16. K. Takamizawa. Y. Ogawa and T. Oyama, *Polym.* J. **14**, 1403 (1982)

17. W. Piesczek, G. R. Strobl and K. Malzahn, *Acta Cryst.* **B30**, 1278 (1974)